Towards combined quantum bit detection and spatial tracking using an arrayed single-photon sensor

Towards combined quantum bit detection and spatial tracking using an arrayed single-photon sensor

Ross Donaldson,[1,*] Dmytro Kundys,[1] Aurora Maccarone,[1] Robert Henderson,[2] Gerald S. Buller,[1] Alessandro Fedrizzi, [1]

1. Scottish Universities Physics Alliance, Institute of Photonics and Quantum Sciences, School of Engineering and Physical Sciences, Heriot-Watt University, David Brewster Building, Edinburgh EH14 4AS, UK.

2. Integrated Micro and Nano Systems, Electronics and Electrical Engineering, School of Engineering, The University of Edinburgh, Edinburgh EH9 3JL, UK.

**Correspondence: R.Donaldson@hw.ac.uk*

Abstract: Experimental quantum key distribution through free-space channels requires accurate pointing-and-tracking to co-align telescopes for efficient transmission. The hardware requirements for the sender and receiver could be drastically reduced by combining the detection of quantum bits and spatial tracking signal using two-dimensional single-photon detector arrays. Here, we apply a two-dimensional CMOS single-photon avalanche diode detector array to measure and monitor the single-photon level interference of a free-space time-bin receiver interferometer while simultaneously tracking the spatial position of the single-photon level signal. We verify an angular field-of-view of 1.28°, and demonstrate a post-processing technique to reduce background noise. The experimental results show a promising future for two-dimensional single-photon detectors in low-light level free-space communications, such as quantum communications.

1. Introduction

1.1. Background

The exchange of quantum bits via optical fiber or free-space links offers the potential of unconditionally verifiably secure quantum key distribution (QKD) for sharing encryption keys between two [1,2] or more [3] parties, unforgeable digital signatures [4,5], secure bit commitment [6], digital fingerprinting [7], oblivious transfer [8], and more.

State-of-the-art QKD using point-to-point fiber links has been demonstrated over distances of several hundreds of kilometers [9–13] in laboratory settings, and over metropolitan distances in deployed dark-fiber networks [14,15]. Optical loss in fibers leads to an exponential decay in secret key rates. Expanding terrestrial fiber QKD beyond point-to-point would therefore require trusted quantum repeater nodes [16,17]. Since quantum repeaters are still far from a mature technology, the fastest route to global quantum networks will be to connect separate metropolitan networks via long distance free-space channels and trusted quantum satellite nodes [18].

Line-of-sight free-space QKD has been developed in parallel to fiber-based systems, with initially static terrestrial links over increasing distances [19,20] and development towards day-time operation [21,22]. In addition, demonstrations and system verification tests have been carried out with mobile platforms, for example ground vehicles [23], aerial platforms [24–26], and a range of in-orbit satellites [27–34]. Due to the unguided and turbulent nature of free-space channels, optical beacons and spatial position sensors are required to actively co-align the transmitter and receiver telescopes during communications, in order to minimize losses in the optical link [35].

Here we demonstrate the feasibility of simultaneous detection of the temporal information encoded in single-photon per clock-cycle level optical pulses as well as their spatial position for telescope pointing-and-tracking. We implement a free-space time-bin receiver interferometer with an optical relay to address wave-front distortion [36] and employ a two-dimensional (2D) silicon-complementary metal–oxide–semiconductor (CMOS) single-photon avalanche diode (SPAD) array with picosecond time-of-arrival resolution for signal detection. Combined signal detection with a single device reduces system complexity and relaxes the size, weight, and power (SWAP) demands on single-photon level receivers, such as those used in QKD. Satellites in particular have a severely restricted SWAP allowance [37] and could therefore greatly benefit from a rollout of future-generation CMOS SPAD arrays.

1.2. Free-space time-bin quantum key distribution

In free-space QKD, polarization is typically used for the encoding due to the robustness of polarization to atmospheric transmission [38], and the relative ease of implementation. A drawback is the need to actively maintain a common polarization basis between a quickly moving sender and stationary receiver. Time-bin QKD protocols do not have this requirement, and they have advantages in terms of SWAP, especially for the transmitter, which can be integrated onto a chip [39]. A number of time-bin configurations have been implemented [40–43], but in the most common scenario sender and receiver encode and decode their time-bin qubits with a matched unbalanced (or asymmetric) interferometers. Free-space transmission causes optical wave-front and phase distortions due to atmospheric turbulence. In free-space unbalanced interferometers, these distortions will lead to a reduction in the measured interferometric visibility if no correction optics are used [36]. If the interferometry is performed using single-mode fiber, large and varying coupling losses will occur due to the distortions if high performance adaptive optics are not implemented [44,45].

A number of solutions have been demonstrated to overcome the issue of free-space asymmetric interferometry, including the introduction of relay optical elements [31,36], passive spatial-mode correction optics [40], and glass blocks with different refractive indexes [36,46]. All passive designs use optical elements that balance the spatial movement of each of the optical paths, essentially creating a symmetric interferometer in terms of imaging. High visibility time-phase interferometry has been demonstrated with glass blocks of different refractive indexes with a field-of-view (FoV) of up to 3° from normal incidence [46]. The time-bin asymmetric interferometer implemented here was chosen based on reference [36], as the multimode fiber connecting the interferometer output could be easily replaced by the 2D SPAD array.

1.*3. Optical beaconing and 2D single-photon detector array technology*

The system requirements for the beacon are dependent on the accuracy required for effectively aligning the quantum signal to single-photon detectors. The small dimensions of single-pixel single-photon detectors (SPDs) and core-diameter of multimode fiber couplers, typically less than 200 μm, impose stringent requirements for fine pointing-and-tracking in free-space communications. Large area single-pixel SPDs (up to and greater than 500 μm) would relax requirements; however, will suffer from greater detector dark noise from the detector itself and ambient light contamination due to the wider FoV. An array of smaller single-pixel SPDs, rather than a larger single pixel, could counteract the increase in noise through spatial post-processing, proving to be an ideal solution for photon-starved free-space communications. Arrayed superconducting nanowire SPD technology is already being implemented in photon-starved optical communication applications, such as deep-space communications [47].

Due to those recent advances and the inclusion of picosecond resolution time-correlated single-photon counting (TCSPC) capabilities, there is now the realistic possibility of performing pointing-and-tracking with single-photon per bit level optical beacons. With the dual capability of the 2D SPAD array, the need for fine-tracking sensors and high power optical beacons could be relaxed or negated in free-space QKD modules, allowing a reduction in system complexity. In

addition, as free-space links are a versatile channel in quantum networks, if the optical power emitted from the free-space modules can be reduced to or be less than laser safety category Class 1, the number of viable locations for QKD transmitter and receiver modules would substantially increase due to compliance with safety considerations air corridors.

Although the 2D CMOS SPAD detector array technology is promising, there are two main challenges when using the weak optical signal as the optical beacon: the dark count rate of the SPAD pixels; and the detection efficiency of the 2D SPAD arrays.

A high dark count rate reduces the effectiveness of the pointing-and-tracking due to the signal to noise of the image created. In QKD the maximum achievable channel loss is determined by the quantum bit error rate (QBER) of the implementation, to which the dark count rate of the detector will make a contribution, particularly in a high channel loss regime. Single-pixel silicon SPADs are Peltier cooled and typically have dark count rates in the order of 1×10^{-3} Hz/μm^2 when operated at -20°C [48]. In order for 2D SPAD arrays to perform at the equivalent channel loss, individual pixels within the detector array will require comparable dark count rates. Improvements to dark count rate have been proposed and demonstrated through the use of different fabrication techniques [49], active cooling of the SPAD pixels [50,51], and the removal of hot-pixels by post-processing [52]. Ito *et al.* [53] have demonstrated 2D SPAD array pixels with dark count rates 3×10^{-2} Hz/μm^2 at room temperature, only an order of magnitude different from commercial single-pixel SPAD devices when cooled to -20°C.

The detection efficiency places similar constraints on the pointing-and-tracking and QKD channel link budget. Improvements to the overall detection efficiency have already been proposed and demonstrated using microlensing [54,55], different architectures [49,53], altering electric field profile in the multiplication region [56], and analog pixel electronics [57].

1.4. Experimental overview

We first outline the experimental system and operation of the 2D SPAD array, Section 2. Our first demonstration, Section 2.1, applies the 2D SPAD array to the free-space time-bin receiver Michelson interferometer (MI), to demonstrate the capability to monitor the interferometric visibility of a time-bin receiver over a wide angle-of-incidence (AoI) response. Our second experiment demonstrates the capability to capture spatial information of the single-photon level signal using the 2D SPAD array at various spatial resolutions, Section 2.2. The third experiment, Section 2.3, highlights an operational aspect of using a 2D SPD array, where post-processing of pixels can be used to improve the interferometric visibility.

2. Experimental method and set up

Here, the optical system used to demonstrate the single-photon level time-bin interferometric measurement and the operation of the 2D SPAD array is outlined. The same optical system and detector were used in all the experiments described in this paper. The general methodology is explained in this section, however specific methodology related to each experiment, such as operation of the 2D SPAD array, is presented in the related experimental section.

2.1. Time-bin transmitter and receiver interferometer

Our time-bin encoder and transmitter is shown in Figure 1 (a). An asymmetric Mach-Zehnder interferometer (MZI) coherently superposes two time-bin basis states |short⟩ and |long⟩. The decoding at the receiver was performed with an asymmetric MI, which interfered the time-bin signal to attain intensity information while the 2D SPAD array was used to resolve the time-bins. The interference occurs between the two laser pulses: |short⟩ from MZI which takes the long path in MI and the |long⟩ from MZI which takes the short MI path.

The optical transmitter signal was generated from a pulsed *Picoquant* laser source, which provided < 70 *ps* full-width at half-maximum (FWHM) optical pulses at a wavelength of 852 nm. The laser driver was externally triggered by the 2D SPAD array electronic board with a repetition rate of 5 MHz. The transmitter MZI was constructed of polarization-maintaining optical fiber,

Figure 1 (a), implementing a temporal delay between |short⟩ and |long⟩ of 1.33 ns. That time difference was chosen to be greater than the FWHM timing-jitter of the 2D SPAD array (see Appendix A). The output of the transmitter interferometer was attenuated to the single-photon per clock-cycle level using a fiber attenuator, simulating a qubit state that would be sent in QKD.

The output of the transmitter was coupled into free-space through an additional optical fiber and a variable fiber-to-free-space collimation package. The additional optical fiber was used to simulate varying degrees of turbulent channel, similar to how previous experiments simulated multimodal signals [36,46]. A single-mode fiber was used to simulate a non-turbulent free-space channel, and provided the benchmark for performance. To simulate turbulent channel (multimodal) measurement capability, two independent multimode optical fibers, of core-diameters 10 µm and 25 µm, were used to test of the optical receiver at two turbulent levels. The use of multimode fiber cannot simulate all aspects of light propagation through a turbulent atmosphere. Here it is only scintillation (wavefront distortion) and modal dispersion that are present. Optical scattering, another feature of a turbulent channel, could be simulated to some extent by increasing the background light level. A variable collimator was used to collimate the beam width ($1/e^2$) to 0.86 mm for the single-mode fiber output.

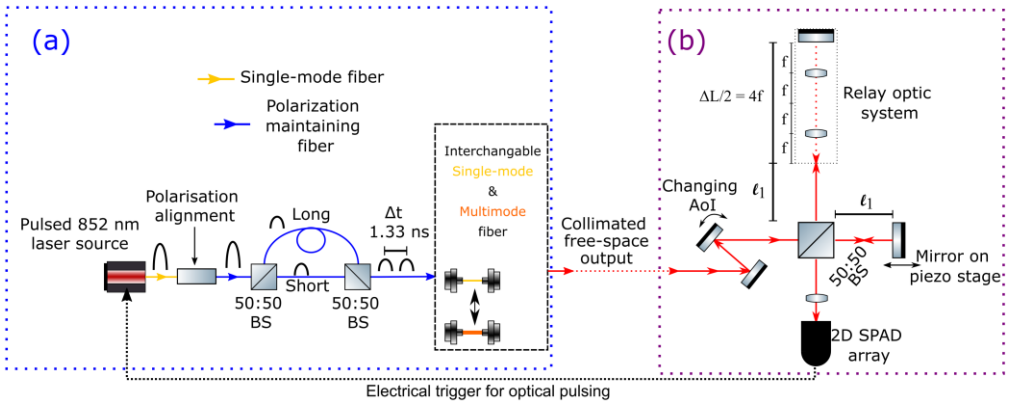

Figure 1 – Experimental scheme for encoding and decoding time-bin signals. (a) The quantum optical transmitter, which simulated time-bin separation of 1.33 ns using an in-fiber asymmetric Mach-Zehnder interferometer. The output of the transmitter was coupled into free-space through interchangeable optical fibers, which were used to simulate different level of turbulence. (b) The quantum optical receiver was a free-space asymmetric Michelson interferometer. The asymmetric arm was constructed with relay optical elements to balance the spatial movement of the two optical paths. The optical output and resultant interferometric visibility were measured using a free-space coupled 2D single-photon avalanche diode (SPAD) detector array. The 2D SPAD array control board was used to electrically trigger the pulsed laser source.

The free-space channel between the transmitter and receiver was 30 cm. The environment was an air-conditioned and temperature stabilized laboratory, which meant the turbulent effects were directly related to the multimode optical fiber transmission. Two tip-tilt alignment mirrors were used to set the initial 0° alignment into the receiver asymmetric interferometer, and a precision dial was used to set known misalignment of the AoI for experiments.

The time-bin interferometer receiver was an asymmetric free-space MI, Figure 1 (b). The short arm of the receiver MI, denoted l_1 in Figure 1 (b), was 12 cm in length one way, to allow for a mirror mounted on a piezoelectric controlled z-translation stage to be included in the optical set up, which allowed for active control of the optical phase shift. The optical time delay between the two optical paths of the receiver was set to 1.33 ns, which corresponded to 40 cm of air. Similar to a previous demonstration [36], the optical path of the optical time delay was constructed from optical relay lens elements, to compensate for the difference in spatial movement of the asymmetric interferometer arms. The relay lens optical system had one-way optical length of 4 times the focal length, *f*, Figure 1 (b). As the interferometer reflects the light back through the

relay system, the total path length was 8*f*. It was the doubling back through the relay lens system, which enabled the compensation of spatial mode. To match the time difference between the successive optical pulses and the free-space interferometer, the focal length of each relay lens was chosen to be 5 cm. The long arm was a total length of 32 cm, one-way, considering 20 cm from the relay lens system and the additional length of the short arm, 12 cm.

At the receiver interferometer's output, a 30 mm focal length convergent lens focused the beam onto the 2D SPAD array plane, which created a focal spot of ~60 µm in diameter for the single-mode, non-turbulent, channel. The 2D SPAD array was aligned to the optical system and fixed in place for the duration of experiments.

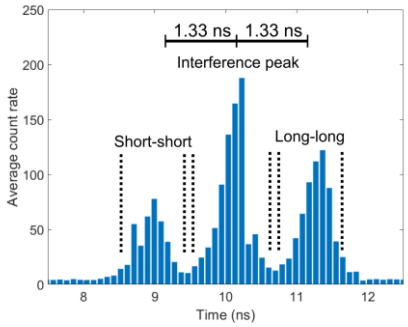

Figure 2 – The interferometric time-bins measured on the 2D single-photon avalanche diode (SPAD) array. The time difference between the time-bins was set to 1.33 ns. The non-interfering (short-short and long-long) and interfering peaks are highlighted. The central interfering peak evolves as the optical phase of the optical paths in the time-bin receiver varies. The histogram was generated from a measurement of 64 illuminated pixels, of which the average was calculated from a 1000 measurement frames each 100 µs exposure.

When in operation, the transmitter and receiver pair with the 2D SPAD array generated the three-peak histogram when averaged over many pulses, shown in Figure 2. The short-short and long-long optical paths of the interferometers do not interfere. The central peak was a superposition of the short-long and long-short paths and thus interferes. The visibility response of the asymmetric interferometer with AoI was monitored using the 2D SPAD array during experiments.

The use of the 2D SPAD array and the 8f asymmetric interferometer enables wide FoV interferometry for photon-starved optical communication applications, such as time-bin QKD. The ability to do both temporal and spatial filtering is not something that can be achieved with a single-pixel single-photon detector. The use of spatial filtering is of particular benefit in wide FoV applications where scattering due to the atmosphere and ambient light will result in an inherently higher noise level.

2.2. Operation of the single-photon avalanche diode 2D array detector

The 2D SPAD array, which can be considered a digital silicon photomultiplier [58], consisted of 1024 silicon CMOS fabricated SPAD pixels in a 32×32 format with overall dimensions of 672 × 672 µm. All pixels were used for measurements in this paper, even those pixels considered detrimental to performance, such as "hot-pixels", which are pixels that have a significantly higher dark count rate [52]. The 2D SPAD array fill factor was 43 %, with a pixel pitch of 21 µm. At the experimental operational wavelength of 852 nm, the single-photon detection efficiency of an individual detector was measured to be 3.5 %. The thin junction fabrication and wavelength choice are the reason for the low efficiency [48]. Operating at a shorter wavelength would increase the detection efficiency. However, 852 nm was chosen, as it was a compromise between detection efficiency and practical considerations of the optical channel [59]. When combined, the fill factor and detection efficiency gave an overall efficiency of 1.5 %. The average time-jitter (measured at FWHM from an independent instrumental response function (IRF) measurement) of all

operational pixels in the 2D SPAD array when measured using the laser source described above, was 245.8 ± 39.5 ps. See Appendix A for more details on the IRF measurement. Figure 2 highlights that the overall 2D SPAD array response was longer than the IRF time-jitter, this is due to optical reflections within the optical receiver and inter-symbol interference.

The electrical readout board and control software allowed acquisition of a 25 ns long event histogram (detection window length defined by the user in software), made of individual 264 timing bins of 94.69 ps duration. The signal sent by the transmitter was known and periodic, which enabled measurements to be represented using a histogram. The length of detection window can be changed to fit an application and is not dependent on the length of the communication channel, as the histogram start time is set by a synchronization pulse. The histogram data was used to generate the results presented in this fixed-distance lab-based experiment. In a real-world implementation, where the distance between the transmitter and receiver are long and dynamic, such as satellite-to-ground, raw time-tag events would be processed with a moving detection window based on a synchronization pulse moving in step with the satellite relative position.

The 2D SPAD array had a maximum achievable photon-counting rate of 1.7G photons/s accumulated over all 1024 pixels. The 2D SPAD array had a maximum histogram rate of 21 k per second, with a readout time of 4.6 μs from the 2D SPAD array chip to the field programmable gate arrays (FPGA) control board. The read-out time occurs after a total number of frames for a complete measurement, rather than between the frames. The minimum acquisition time per frame was 1 μs, capable of recording 1.7 k time-tagged events per selected pixels. More details about the 2D SPAD array design and fabrication can be found in [58].

The detector readout provided accumulated information from all individual pixels, which were activated for a measurement. That meant that individual pixels from the larger accumulation could not then be analyzed independently in post-processing. Individual SPAD pixels activated at the same time acted as an individual large area detector, with the size of the detector area being determined prior to a measurement. It is worth noting that other designs of 2D SPAD arrays have independent pixel post-processing capability [55], but this was not deemed necessary for the experiments described in this paper.

In order to perform a measurement with the 2D SPAD array, a set of pixels were selected and then activated for a pre-determined acquisition time and number of frames. In order to measure the spatial information, the 2D SPAD array was split into grid sections of a defined size. Individual sections of the predefined size of the SPAD array were then activated sequentially, scanning across the entire 2D SPAD array area, similar to a raster scan.

The detector area (672 × 672 μm) and focal length of the asymmetric interferometer receiver (30 mm) gave an angular FoV of 1.28°. More details and a description of the 2D SPAD array characterization can be found in Appendix A.

3. Experimental results

3.1. Single-photon level bit detection with the 2D single-photon detector array

The asymmetric interferometer was used in two different configurations, with and without the relay lens optical elements, to compare the visibility response while varying AoI. The visibility response was recorded for the three interchangeable optical fibers. The AoI was set using the alignment mirror highlighted in Figure 1 (b).

To measure the visibility as the function of AoI, the spatial position of the optical beam on the 2D SPAD array was first identified for each input angle. This was performed by scanning the 2D SPAD array using a 4 × 4 grid and identifying the optical beam position. Each grid section contained 64 pixels. Once the spatial position of the optical beam was identified, one section of the 4 × 4 grid was activated for 1000 frames (frame duration of 100 μs) while the piezoelectric z-translation stage in the receiver interferometer was actively detuned, capturing several interference fringes of optical visibility to estimate the average visibility. There was no dead-time between the frames, as the read-out of data was performed after the measurement. The visibility

of the interferometer was calculated by post-processing the data that recorded the evolution of the central interference peak, see Appendix B for more details.

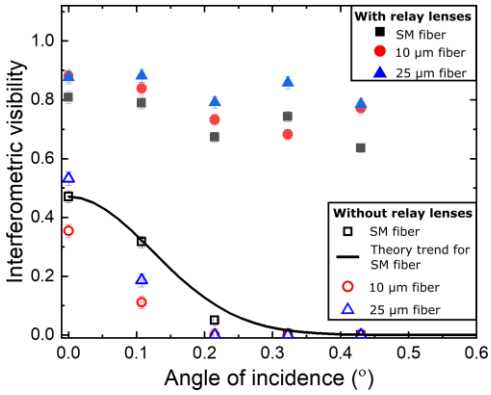

Figure 3 - Comparison of the measured visibility versus angle of incidence for the two Michelson interferometer configurations, with and without corrective relay lens optical elements. The tests involved three optical channels simulated by three different optical fibers, which were collimated into free-space. The solid line highlights the predicted theoretical visibility drop-off with angle of incidence for the single-mode (SM) channel with no relay lenses implemented [60]. It can be seen that when the relay lens optical elements were included in the design, the visibility is considerably more robust to angle of incidence change.

Figure 3 shows a comparison of the visibility, measured using the 2D SPAD array, against AoI for the three optical channels (simulated by the three interchangeable collimated optical fibers), with and without the corrective relay lens optical elements. The AoI range ranged from 0° up to 0.43°.

Without the relay optics, the visibility decreases rapidly with increasing AoI, Figure 3. Even at an AoI of 0°, the visibility is significantly lower without the relay lenses when compared to the other case. Based on theory described in [60], the visibility versus AoI for the single-mode (Gaussian beam profile) channel, is plotted in Figure 3 as the solid black line. The theory takes into account the asymmetry of the interferometer, the optical beam diameter, and AoI. When using the single-mode fiber input, the visibility measurements without relay lenses was generally in agreement with the model proposed in [60]. As expected, the other multimode inputs (10 µm and 25 µm diameter) also showed poor visibility response and a sharp drop in visibility as the AoI was increased.

With relay optics in place, the interference visibility remains high for all three different optical channels, as expected from previous demonstrations [36]. There is a visibility drop-off at large angles of incidence, which is due to fine optical misalignment of the relay optical elements in the receiver. It is clear that the optical relay significantly improves performance for all values of AoI and for different input fibers.

The results in Figure 3 demonstrate that a 2D SPAD array can be used to monitor the visibility evolution of an asymmetric interferometer at the single-photon level over a large AoI, an essential step towards permitting the measurement of quantum bit information in a QKD protocol.

3.2. Spatial information measurement of the single-photon level optical beam

A potential benefit of using a 2D SPAD array over the single-pixel counterpart is the ability to measure both the TCSPC events as well as spatial information of the detected photon, which corresponds to the unpredictable AoI in a free-space QKD receiver in the presence of atmospheric turbulence. Due to the read-out of the 2D SPAD array used in this experiment, the 2D SPAD array was scanned electronically to capture spatial information. This electronic scanning of read-out

information simulates how the spatial information would be acquired if the 2D SPAD array utilised a read-out architecture capable of processing each SPAD pixel independently.

To demonstrate the measurement of spatial information, the 2D SPAD array was set into four configurations. Each configuration set a different spatial resolution of the 2D SPAD array. The four configurations split the 2D SPAD array into 1×1, 2×2, 4×4, and 8×8 grids, which divided the 1024 individual pixels equally amongst each section of the grids. The sections were chosen to simulate a large single pixel SPAD detector, a quadrature detector, and two higher resolution 2D array detectors.

All measurements of spatial information were carried out in two steps. The first step was a background measurement, to record the average background counts resulting from detector dark events in the 2D SPAD array and contributions from other ambient light sources, for each of the specified pixel sections. The second step was a measurement with the quantum optical signal incident on the 2D SPAD array. The experiment was carried out with the same optical system outlined in Figure 1, including the interference measurements. However, the interferometers were stabilized to ensure consistent signal power. The single-mode, non-turbulent, channel was used over the multimode channel, but the same results are expected independent of channel. Each spatial resolution measurement was a full scan of the 2D SPAD array for a specified configuration. The sections were activated for 5 frames, each frame having an acquisition time of 100 μs. There was no dead-time between the frames of measurement, however there was a read-out dead-time (4.6 μs) between the sections due to read-out of information from the chip to the FPGA. The background noise measurement was subtracted from the signal measurement during post-processing, to enable easy identification of the signal.

Figure 4 shows the resultant measurements identifying the spatial position of the optical beam for a 1×1 (a), 2×2 (b), 4×4 (c), and 8×8 (d) grids. As can be seen in Figure 4, as the grid resolution increases, the precise location of the optical beam can be identified more accurately. However, a spatial resolution as low as 2×2 section is sufficient for identifying the approximate position of the optical beam. 2×2 (quadrature style) detectors are commonly used in free-space laser communications for pointing and tracking [61], and the experiment demonstrates that a single-photon sensitive equivalent could be implemented.

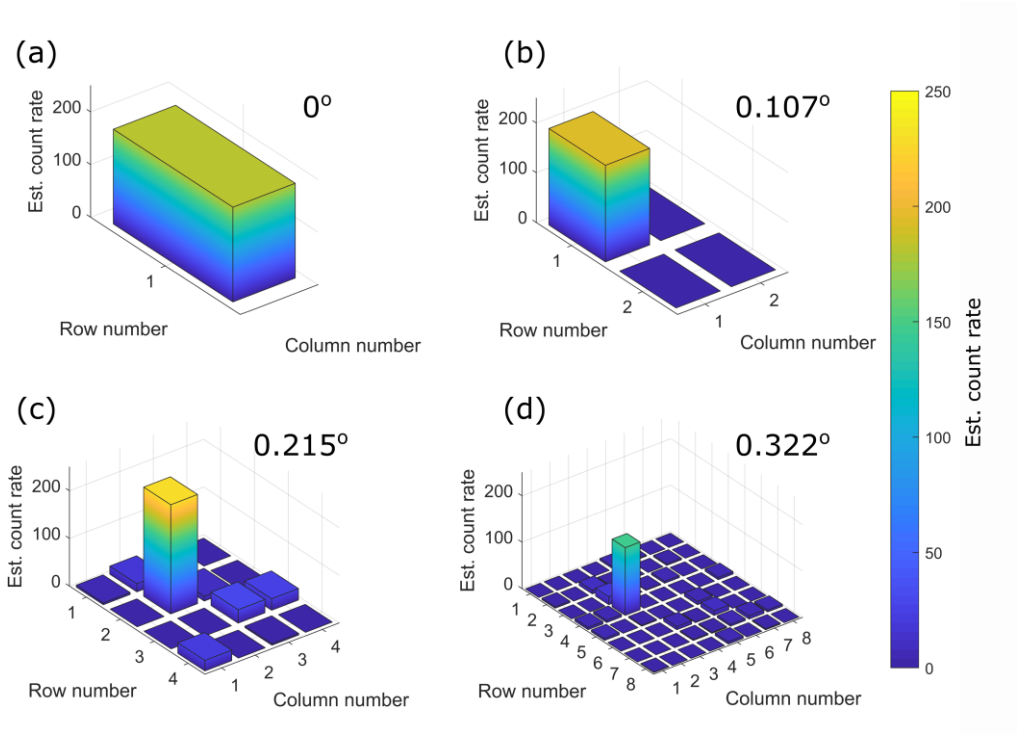

Figure 4 – Capturing spatial information using four different configurations of 2D single-photon avalanche diode (SPAD) array. The 2D SPAD array was split into sections of pixels that were activated independently to capture spatial information. As can be seen the resolution of the spatial measurement can be improved by increasing the section number. Grid row and column number refer to the position on the physical 2D SPAD array.

The focal spot diameter of the optical beam on the 2D SPAD array was designed to be 60 µm, based on the initial beam width for the single-mode channel and focal length of the final lens. With a single-pixel SPAD detector, verifying the single-photon level spot size would require precise spatial positioning mechanisms, and a time-consuming process to move the SPAD into place. Here, direct measurement of the focal spot size using the 2D SPAD array can be performed by taking advantage of the spatial measurement. The 8 × 8 grid, where each section is composed of a 16 pixel square, has a section dimension of 80 × 80 µm. It can be seen from Figure 4 (d), that the beam is focused within one section, demonstrating that the 2D SPAD array was well positioned at the focal point of the lens, and that the spot size was less than 80 µm.

To verify the angular FoV of the detector and the angular movement set for experimental measurements, the spatial movement with AoI was measured using the 2D SPAD array. Figure 5 shows the spatial movement for an 8 × 8 scan as the AoI was changed. It can be seen that as the AoI changes, so does the position of the spatial position on the 2D SPAD array. The spatial position was measured for set angles of incidence 0° (a), 0.107° (b), 0.215° (c), and 0.322° (d).

The angular FoV of the 2D SPAD array was calculated to be 1.28°, based on the detector square dimensions (672 µm) and the focal length of the final lens (30 mm). The angular setting ranged from 0° to 0.322°, which is ~25 % of the angular FoV. As the AoI increases from 0° to 0.322°, the grid position changes, capturing optical beam movement. It starts in position row 4 column 3, Figure 5 (a), and ends in row 6 column 3 Figure 5 (d). The beam movement of approximately 2 rows of the 8 × 8 grid, corresponding to 160 µm movement, equal to 25 % of the overall 2D SPAD array linear dimension.

As the fill-factor of the 2D SPAD array used was not 100%, it is inevitable that light will fall between the active pixels while performing the scan, leading to a reduction in the measured signal

when light falls between the pixels. This intensity fluctuation is most evident in Figure 5, due to the AoI changes. By increasing the fill-factor of the SPAD detector array, we hope to reduce these intensity fluctuations.

The measurements from this section demonstrate that spatial position of a single-photon level intensity optical signal can be captured using 2D SPAD array technology. The measurements also verify the AoI set during experiments and the FoV of the detector and lens combination. The wide FoV of the 2D SPAD array detector can be taken advantage of in time-bin QKD, where the angular response of the optical receiver is also wide.

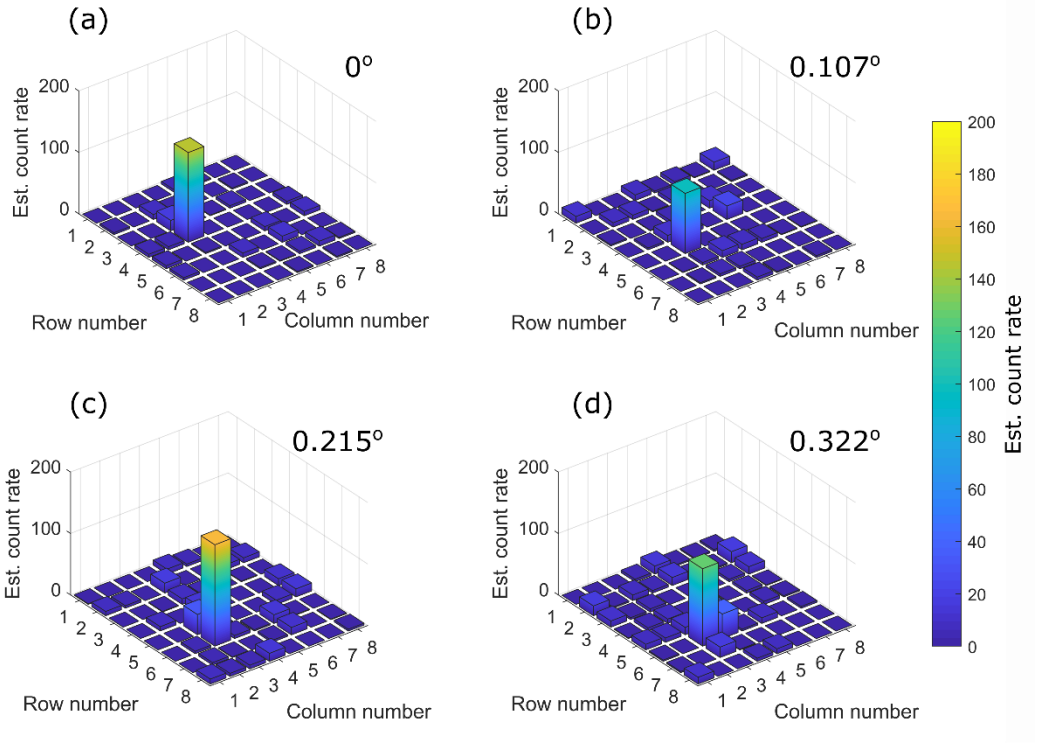

Figure 5 - Movement of the optical beam across the 2D single-photon avalanche diode (SPAD) detector array. Each subplot corresponds to an angle of incidence set, (a) 0°, (b) 0.107°, (c) 0.215°, and (d) 0.322°. Those angles of incidence calculated based on the specified response of a tip-tilt mirror.

3.3. Pixel selection to reduce signal-to-noise ratio.

Visibility is an essential measurement for the security of time-bin QKD protocols [41]. Low visibility performance in time-bin protocols will lead to an increase in key rate reduction cause by post-processing algorithms, or even protocol failure [2]. Although this paper has highlighted the benefits of using 2D SPAD array technology, the use of multiple, and many, SPAD pixels inevitably leads to an increase in the detector background noise, which will increase the quantum bit error rate (QBER) of a QKD protocol, reducing protocol performance.

The 2D SPAD array enables a wide FoV receiver due to the larger detector dimensions. However, because the optical beam is focused on the 2D SPAD array, there are pixels in the array that are not illuminated by the single-photon level signal but contribute to the background noise. Post-selecting pixels, which contribute to the final single-photon level measurement, could enable better performance from the same SPAD array. This experiment investigates the improvement in measured visibility by reducing the number of pixels included in acquisition of the measurement.

For each AoI, the visibility was measured, using the same methodology as Section 3.1, for various pixel grid sizes, defined in Section 3.2.

Figure 6 shows the interferometric visibility versus AoI for different pixel grid sizes. As can be seen in Figure 6, as the number of active SPAD pixels incorporated in the visibility measurement decreases, the visibility measured increases. The optical beam from the interferometer is focused down to 60 µm, meaning the majority of the 2D SPAD array area is not receiving photons for the visibility measurement. Those excess pixels add additional, and unwanted, noise to the visibility measurement, essentially reducing the visibility.

The result highlights that incorporating all the pixels in the 2D SPAD array for one single-photon level channel would not be beneficial, unless the noise associated with each pixel was negligible. The wide FoV of the detector would also lead to additional background noise from the channel, which would further reduce the visibility. While using this protocol, the whole detector array could be used to collect single-photon level bits, taking advantage of the wide FoV, allowing the beam to wander across the array during measurements. The data, which will have the spatial position of the optical beam on the 2D SPAD detector, could then be post-processed to only include a select number of pixels for the final visibility measurement. The post-selection would reduce the contributions of temporal and spatially scattered light from the optical signal as it propagates through a turbulent channel.

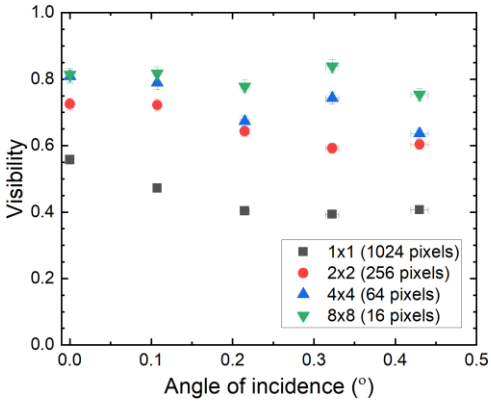

Figure 6 – Interferometric visibility measured for different section sizes. The section sizes for the 2D single-photon avalanche diode (SPAD) array are highlighted in the legend. It can be seen that as the number of sections increases, so does the visibility of the interferometric measurement.

The experiment shows that the reconfigurable flexibility of 2D SPAD array enables the optimization between two extreme conditions to obtain high visibility single-photon measurement while still maintaining a wide FoV spatial measurement. However, in practice, that functionality would require independent read-out circuitry for each pixel to enable the post-processing. Here the spatial position was identified before narrowing down for an active measurement with a specific section size.

4. Conclusion

This paper set out to demonstrate the feasibility of combining the measurements of single-photon level bit information and optical spatial position using an arrayed single-photon sensor. The combined detection capability is beneficial for a free-space single-photon level communications, such as QKD, alleviating the requirement for high-power optical alignment beacons, as the fine pointing and tracking detection could be performed using the single-photon level signal and a 2D SPAD array (or more generally a 2D SPD array). We conducted three experimental demonstrations to show the practical feasibility, implementing a 32 × 32 pixel Si-CMOS 2D SPAD array and a time-bin receiver interferometer.

In the first experiment, the capability to measure and monitor single-photon level visibility of a time-bin receiver interferometer, a critical measurement for time-bin QKD protocols, was demonstrated. All measurements required the spatial information to be tracked as the AoI was changed. The robustness of the interferometer design to changes in AoI and wave-front distortions was also demonstrated.

The single-photon level spatial position tracking was demonstrated in the second experiment. We showed that a 2D SPAD array can be configured for various pixel resolutions, creating higher or lower spatial resolution detectors for spatial tracking. The 2D SPAD was also used to verify the angular FoV of the optical system (1.28°) and to track known spatial misalignment.

In the final experiment, we showed that the signal-to-noise of a quantum measurement can be improved by processing the spatial position of the single-photon level optical signal and then down-selecting the number of individual 2D SPAD array pixels used for the visibility measurement. This can be performed by post-processing the measurement data, provided the 2D SPAD array has the ability to independently read-out each pixel.

The experiments from this paper have demonstrated the promising future for SPAD detectors, and more generally SPD, array technology in photon-starved free-space optical communications, such as QKD. With many teams working on SPD array technology, continuing advances will further improve the prospects for SPD detector arrays in photon-starved free-space optical communications. Key challenges to enable applications in free-space QKD are already being addressed, such as fabrication of 2D SPAD arrays with inherently low dark count rate per pixel, even before active cooling [49,51,53,57], and increasing the detection efficiency [49,53–57]. With the reduction in dark count rate per pixel and improvements in detection efficiency for specific wavelengths, applications in QKD for 2D SPAD arrays will be more realistic, especially with the inclusion of specialized electronics to enable QKD processing.

Appendix A: 2D single-photon avalanche diode array characterization

This appendix provides additional details on the 2D single-photon avalanche diode (SPAD) detector array, which can be considered a digital silicon photomultiplier, implemented in the main paper. Understanding the measurement capabilities of the 2D SPAD array was a vital aspect when designing quantum key distribution (QKD) receiver's asymmetric interferometer [42]. The detector timing-jitter [48], defines how close in time the two adjacent time-bins can be [62], and therefore sets the minimum size of the asymmetry of the Michelson interferometer (MI) and upper bound for time-bin resolution. The dark count rate per pixel effects measurement performance, and thus the overall performance of QKD protocol. Other detector characteristics [48], such as afterpulsing or pixel cross-talk, were not included in this analysis.

Methods for dark count rate and timing-jitter measurements

For measurements of both timing-jitter and dark count rate, each individual pixel was activated for 1 ms per acquisition for one frame. The 2D SPAD array was scanned multiple times to give a statistical average and standard deviation for timing-jitter and dark count rate. Both measurements were carried out in a dark room, and experiments, where possible, were activated remotely to reduce ambient light levels at the start of experiments.

To measure the dark count rate per second, the dark count per 1 ms was multiplied to give 1s acquisition. To reduce potential light background ambient light levels further, the detector was housed inside a lightproof container.

The timing-jitter of the 2D SPAD array was measured in the following way. A pulsed laser source, providing $< 70\,ps$ FWHM optical pulses, at a wavelength of 852 nm, was used to illuminate the 2D SPAD array through an engineered diffusor in free-space. The engineered diffusor created a circular top-hat intensity profile, and the detector was placed at a distance where the intensity profile was relatively even across the whole 2D SPAD array. The laser source was electrically pulsed at an operational clocking frequency of 5 MHz. The histogram data generated for each pixel, example in Figure 7, was post-processed to identify the peak intensity and the FWHM timing-jitter using a Gaussian fitting function.

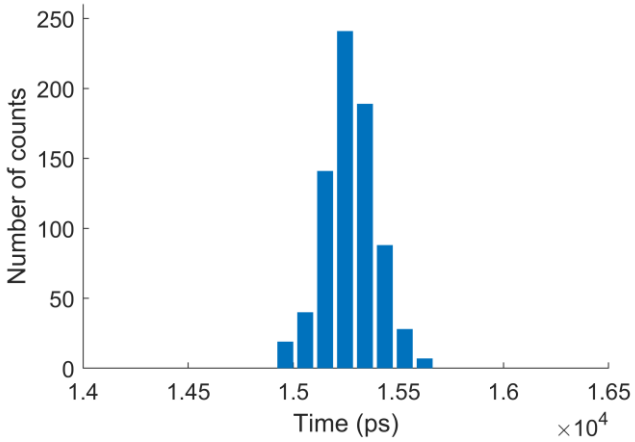

Figure 7 – Timing histogram of a single pixel from the 2D single-photon avalanche diode (SPAD) detector array. The figure zooms in on the single peak in the histogram where the Gaussian fit was applied to the data.

Characterization results and discussion

The dark count rate for each pixel is shown in Figure 8 (a), highlighting the spatial distribution of the dark count rate over the 2D array. It can be seen that the dark count rate per pixel is randomly distributed throughout the 2D array. The minimum dark count rate was found to be $4.05 \times 10^4 \pm 6.18 \times 10^3$ counts per second, while the maximum was $2.64 \times 10^7 \pm 3.34 \times 10^5$ counts

per second. The average over all 1024 pixels was found to be $1.39 \times 10^6 \pm 7.56 \times 10^4$ counts per second. The three orders of magnitude difference in minimum and maximum is due to the presence of hot-pixels, which have a substantially higher dark count rates than other pixels [52].

Reducing the dark count rate is essential for QKD applications, as excess noise contributes to the quantum bit error rate (QBER) of the protocol, limiting the loss budget available and reducing the secret key rate. The limited loss budget is analogous to reducing the achievable transmission distances. It should be noted that the average dark count rate could be reduced if cooling was applied to the detector chip. Even when cooling the 2D SPAD array chip, hot-pixels are still an issue. Identifying hot-pixels within the 2D array is essential to identifying and removing those troublesome pixels. The authors of [52] note that up to 20% of a 2D SPAD array could be hot-pixels.

The dark count rate measurements were re-analyzed to identify hot pixels in the 2D SPAD array, based on the methods described in [52]. A histogram of number of pixels versus dark count rate with a fitted log-normal distribution, Figure 8 (b), shows that the distribution is elongated, as there are a number of pixels that have a significantly higher dark count rate. Reference [52] identifies a pixel as hot if it has a dark count rate larger than 3σ of the distribution average. Using that definition, it was found that 7 % of the pixels in the 2D SPAD array characterized were termed "hot". These pixels were not removed or post-selected out during experiments within the main paper, as it was deemed more representative of the overall performance to include all pixels in measurements for this feasibility study.

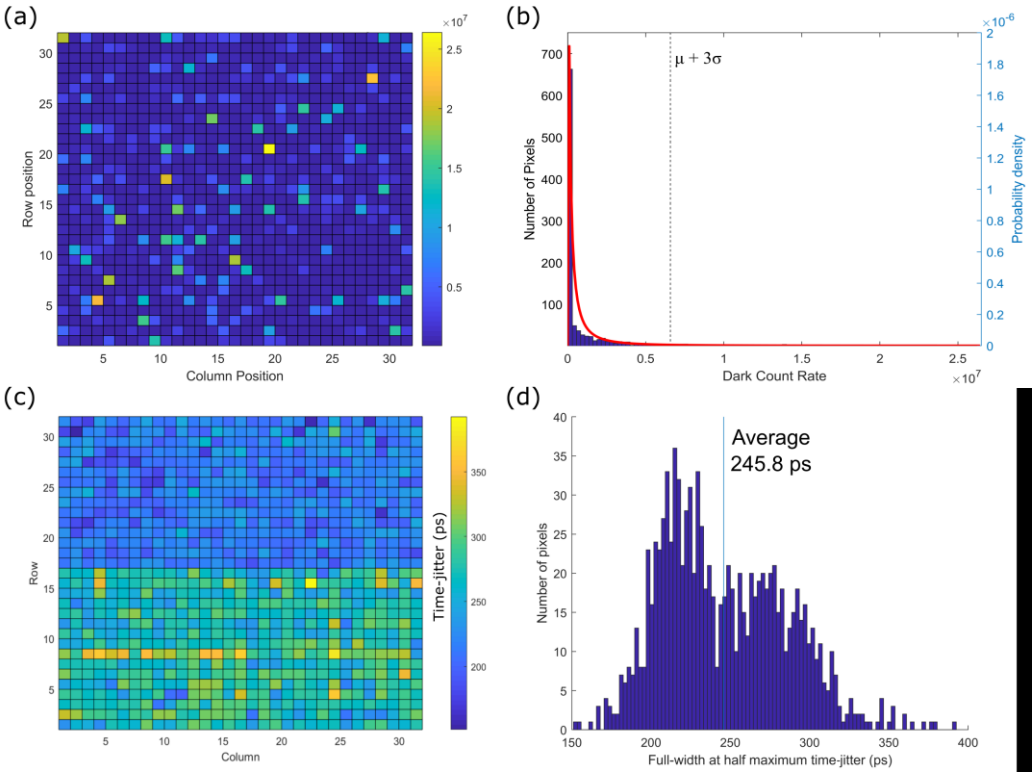

Figure 8- Single-photon avalanche diode 2D detector array dark count rate response for each pixel in the array (a), the dark count rate distribution to identify hot pixel (b), the full-width at half-maximum (FWHM) timing-jitter per pixel in the array (c), and the distribution of timing-jitter (d).

Figure 8 (c) shows the timing-jitter measured for each pixel in the 2D array at the position in the 2D SPAD array. As can be seen, and unlike the dark count rate measurements, there is a clear split in measured timing-jitter between the top and bottom halves of the chip. The splitting is also

evident in Figure 8 (d). The split in timing-jitter is due to signal routing of the array pixels to the time-to-digital converter (TDC). There was a shorter path from one-half of the chip to the TDC, leading to a shorter timing-jitter. The longer path would cause slower edges on the response, leading to an increased spread in timing. The FWHM timing-jitter values range from 151 *ps* to 393 *ps*, and the distribution can be seen in Figure 8 (d). As well as spatial position, reference [58] highlights that the timing-jitter response is also dependent on the number of pixels activated for a measurement. However, that effect on the quantum bit measurement was not extensively studied. The average timing-jitter was found to be 245.8 ± 39.5 *ps*. As the laser pulse duration was <70 *ps*, the stated time-jitter values were dominated by the effects of the detector itself.

During the post-processing of the timing jitter, the central peak position per pixel was analyzed using the information from the Gaussian fitting function in MATLAB. It was found that 88% of the central positions occurred in the same time bin (width 94.69 ps), while 10% occurred in the bin before and 2% in the bin after. This highlights that there was a relative time delay between a small number of the pixels in the array. In this paper, the time interval between the optical pulses was much larger than the relative time delay, which means the effects on these experiments are negligible. However, this time-delay is fixed and can be characterized for any 2D SPAD array fabricated, meaning post-processing corrections can be made routinely to individual detector timings as they are in single-photon LIDAR measurement using arrayed detectors [63], reducing any impact on time-correlation measurements in QKD.

The timing-jitter measurements were critical for the design of the quantum optical receiver. Due to the extended timing-jitter tail of single-photon detectors [62], the optical time difference needs to be greater than the measured timing-jitter to reduce the QBER. In the case of the 2D SPAD array used for this paper, the average full width at 10 % maximum was found to be ~1 *ns*. This set the minimum time difference to be ≥ 1 *ns*, which is ~30 *cm* propagation in air. The optical system for the main paper was designed with a time delay of 1.33 *ns* due to this detector characteristic.

Appendix B: Calculation of interferometer visibility

The interferometric visibility was calculated using the following method after data was acquired using the method described in 3.1. The data output for analysis was 1000 frames (histogram plots), each acquisition being 100 μs long. The central, interfering, peak in the histogram was first identified by summing all 1000 histogram frames together, followed by a peak finder function in MATLAB to identify the central peak. The peak finder function was verified visually. After the central peak identification, a time-gating window of 500 *ps* was applied to each histogram, the center of the time-gate was positioned at the middle of the interfering peak. For each frame, the number of photon events within the time-gated window were summed together to give a count rate (CR). As the interferometer was actively tuned to capture multiple interference fringes, over the 1000 frames the CR reaches a maximum (CR_{Max}) and minimum value (CR_{Min}). The interferometric visibility of the interferometer was calculated using Eq. (1).

$$\mathrm{V} = \frac{(\mathrm{CR_{Max}} - \mathrm{CR_{Min}})}{(\mathrm{CR_{Max}} + \mathrm{CR_{Min}})} \quad (1)$$

The data associated with this work can be downloaded from the Heriot-Watt University data archive at XXXXXXXXXXX.

5. Funding

This research was funded by; the UK Engineering and Physical Sciences Research Council (EPSRC) through projects EP/N002962/1, EP/K015338/1, EP/T001011/1, EP/T00097X/1 and EP/N003446/1; and the Royal Academy of Engineering through an Early Career Research Fellowship No. RF\201718\1746.

6. Acknowledgements

We would like to acknowledge Thomas Jennewein and Tarek Al Abbas for useful discussions.

7. Disclosure

The authors declare that there are no conflicts of interest related to this article.

8. References

1. W. Tittel, H. Zbinden, and N. Gisin, "Quantum cryptography," Rev. Mod. Phys. **74**(1), 145–195 (2002).
2. S. Pirandola, U. L. Andersen, L. Banchi, M. Berta, D. Bunandar, R. Colbeck, D. Englund, T. Gehring, C. Lupo, C. Ottaviani, J. Pereira, M. Razavi, J. S. Shaari, M. Tomamichel, V. C. Usenko, G. Vallone, P. Villoresi, and P. Wallden, "Advances in Quantum Cryptography," arXiv 1–118 (2019).
3. M. Proietti, J. Ho, F. Grasselli, P. Barrow, M. Malik, and A. Fedrizzi, "Experimental quantum conference key agreement," arXiv 1–10 (2020).
4. R. J. Collins, R. J. Donaldson, V. Dunjko, P. Wallden, P. J. Clarke, E. Andersson, J. Jeffers, and G. S. Buller, "Realization of quantum digital signatures without the requirement of quantum memory," Phys. Rev. Lett. **113**(4), 040502 (2014).
5. R. J. Donaldson, R. J. Collins, K. Kleczkowska, R. Amiri, P. Wallden, V. Dunjko, J. Jeffers, E. Andersson, and G. S. Buller, "Experimental demonstration of kilometer-range quantum digital signatures," Phys. Rev. A **93**(1), (2016).
6. Y. Liu, Y. Cao, M. Curty, S.-K. Liao, J. Wang, K. Cui, Y.-H. Li, Z.-H. Lin, Q.-C. Sun, D.-D. Li, H.-F. Zhang, Y. Zhao, T.-Y. Chen, C.-Z. Peng, Q. Zhang, A. Cabello, and J.-W. Pan, "Experimental Unconditionally Secure Bit Commitment," Phys. Rev. Lett. **112**(1), 010504 (2014).
7. F. Xu, J. M. Arrazola, K. Wei, W. Wang, P. Palacios-Avila, C. Feng, S. Sajeed, N. Lütkenhaus, and H.-K. Lo, "Experimental quantum fingerprinting with weak coherent pulses," Nat. Commun. **6**, 8735 (2015).
8. R. Amiri, R. Stárek, M. Mičuda, L. Mišta, M. Dušek, P. Wallden, and E. Andersson, "Imperfect 1-out-of-2 quantum oblivious transfer: bounds, a protocol, and its experimental implementation," arXiv 1–20 (2020).
9. B. Korzh, C. C. W. Lim, R. Houlmann, N. Gisin, M. J. Li, D. Nolan, B. Sanguinetti, R. Thew, and H. Zbinden, "Provably secure and practical quantum key distribution over 307 km of optical fibre," Nat. Photonics **9**(3), 163–168 (2015).
10. H.-L. Yin, T.-Y. Chen, Z.-W. Yu, H. Liu, L.-X. You, Y.-H. Zhou, S.-J. Chen, Y. Mao, M.-Q. Huang, W.-J. Zhang, H. Chen, M. J. Li, D. Nolan, F. Zhou, X. Jiang, Z. Wang, Q. Zhang, X.-B. Wang, and J.-W. Pan, "Measurement-Device-Independent Quantum Key Distribution Over a 404 km Optical Fiber," Phys. Rev. Lett. **117**(19), 190501 (2016).
11. D. Stucki, N. Walenta, F. Vannel, R. T. Thew, N. Gisin, H. Zbinden, S. Gray, C. R. Towery, and S. Ten, "High rate, long-distance quantum key distribution over 250 km of ultra low loss fibres," New J. Phys. **11**, (2009).
12. S. Wang, W. Chen, J.-F. Guo, Z.-Q. Yin, H.-W. Li, Z. Zhou, G.-C. Guo, and Z.-F. Han, "2 GHz clock quantum key distribution over 260 km of standard telecom fiber.," Opt. Lett. **37**(6), 1008–10 (2012).
13. J.-P. Chen, C. Zhang, Y. Liu, C. Jiang, W. Zhang, X.-L. Hu, J.-Y. Guan, Z.-W. Yu, H. Xu, J. Lin, M.-J. Li, H. Chen, H. Li, L. You, Z. Wang, X.-B. Wang, Q. Zhang, and J.-W. Pan, "Sending-or-Not-Sending with Independent Lasers: Secure Twin-Field Quantum Key Distribution Over 509 km," Phys. Rev. Lett. **124**(7), 70501 (2019).
14. M. Sasaki, "Quantum networks: where should we be heading?," Quantum Sci. Technol. **2**(2), 020501 (2017).
15. M. Sasaki, M. Fujiwara, H. Ishizuka, W. Klaus, K. Wakui, M. Takeoka, S. Miki, T. Yamashita, Z. Wang, A. Tanaka, K. Yoshino, Y. Nambu, S. Takahashi, A. Tajima, A. Tomita, T. Domeki, T. Hasegawa, Y. Sakai, H. Kobayashi, T. Asai, K. Shimizu, T. Tokura, T. Tsurumaru, M. Matsui, T. Honjo, K. Tamaki, H. Takesue, Y. Tokura, J. F. Dynes, A. R. Dixon, A. W. Sharpe, Z. L. Yuan, A. J. Shields, S. Uchikoga, M. Legré, S. Robyr, P. Trinkler, L. Monat, J.-B. Page, G. Ribordy, A. Poppe, A. Allacher, O. Maurhart, T. Länger, M. Peev, and A. Zeilinger, "Field test of quantum key distribution in the Tokyo QKD Network.," Opt. Express **19**(11), 10387–409 (2011).
16. H. J. Kimble, "The quantum internet.," Nature **453**(7198), 1023–30 (2008).
17. Y. Mao, B.-X. Wang, C. Zhao, G. Wang, R. Wang, H. Wang, F. Zhou, J. Nie, Q. Chen, Y. Zhao, Q. Zhang, J. Zhang, T.-Y. Chen, and J.-W. Pan, "Integrating quantum key distribution with classical communications in backbone fiber network," Opt. Express **26**(5), 6010 (2018).
18. R. Bedington, J. M. Arrazola, and A. Ling, "Progress in satellite quantum key distribution," npj Quantum Inf. **3**(1), 30 (2017).
19. T. Schmitt-Manderbach, H. Weier, M. Fürst, R. Ursin, F. Tiefenbacher, T. Scheidl, J. Perdigues, Z. Sodnik, C. Kurtsiefer, J. G. Rarity, A. Zeilinger, and H. Weinfurter, "Experimental demonstration of free-space decoy-state quantum key distribution over 144 km," Phys. Rev. Lett. **98**(1), 1–4 (2007).
20. T. Scheidl, R. Ursin, A. Fedrizzi, S. Ramelow, X.-S. Ma, T. Herbst, R. Prevedel, L. Ratschbacher, J. Kofler, T. Jennewein, and A. Zeilinger, "Feasibility of 300 km quantum key distribution with entangled states," New J. Phys. **11**(8), 085002 (2009).
21. S.-K. Liao, H.-L. Yong, C. Liu, G.-L. Shentu, D.-D. Li, J. Lin, H. Dai, S.-Q. Zhao, B. Li, J.-Y. Guan, W. Chen, Y.-H. Gong, Y. Li, Z.-H. Lin, G.-S. Pan, J. S. Pelc, M. M. Fejer, W.-Z. Zhang, W.-Y. Liu, J. Yin, J.-G.

Ren, X.-B. Wang, Q. Zhang, C.-Z. Peng, and J.-W. Pan, "Long-distance free-space quantum key distribution in daylight towards inter-satellite communication," Nat. Photonics **11**(8), 509–513 (2017).

22. M. Avesani, L. Calderaro, M. Schiavon, A. Stanco, C. Agnesi, A. Santamato, M. Zahidy, A. Scriminich, G. Foletto, G. Contestabile, M. Chiesa, D. Rotta, M. Artiglia, A. Montanaro, M. Romagnoli, V. Sorianello, F. Vedovato, G. Vallone, and P. Villoresi, "Full daylight quantum-key-distribution at 1550 nm enabled by integrated silicon photonics," arXiv **1**, 1–7 (2019).
23. J.-P. Bourgoin, B. L. Higgins, N. Gigov, C. Holloway, C. J. Pugh, S. Kaiser, M. Cranmer, and T. Jennewein, "Free-space quantum key distribution to a moving receiver," Opt. Express **23**(26), 33437 (2015).
24. J. Wang, B. Yang, S. Liao, L. Zhang, Q. Shen, X.-F. Hu, J. Wu, S. Yang, H. Jiang, Y. Tang, B. Zhong, H. Liang, W. Liu, Y. Hu, Y. Huang, B. Qi, J. Ren, G.-S. Pan, J. Yin, J. Jia, Y.-A. Chen, K. Chen, C. Peng, and J. Pan, "Direct and full-scale experimental verifications towards ground–satellite quantum key distribution," Nat. Photonics **7**(5), 387–393 (2013).
25. C. J. Pugh, S. Kaiser, J. Bourgoin, J. Jin, N. Sultana, S. Agne, E. Anisimova, V. Makarov, E. Choi, B. L. Higgins, and T. Jennewein, "Airborne demonstration of a quantum key distribution receiver payload," Quantum Sci. Technol. **2**(2), 024009 (2017).
26. S. Nauerth, F. Moll, M. Rau, C. Fuchs, J. Horwath, S. Frick, and H. Weinfurter, "Air-to-ground quantum communication," Nat. Photonics **7**(5), 382–386 (2013).
27. J. Yin, Y. Cao, Y.-H. Li, S.-K. Liao, L. Zhang, J.-G. Ren, W.-Q. Cai, W.-Y. Liu, B. Li, H. Dai, G.-B. Li, Q.-M. Lu, Y.-H. Gong, Y. Xu, S.-L. Li, F.-Z. Li, Y.-Y. Yin, Z.-Q. Jiang, M. Li, J.-J. Jia, G. Ren, D. He, Y.-L. Zhou, X.-X. Zhang, N. Wang, X. Chang, Z.-C. Zhu, N.-L. Liu, Y.-A. Chen, C.-Y. Lu, R. Shu, C.-Z. Peng, J.-Y. Wang, and J.-W. Pan, "Satellite-based entanglement distribution over 1200 kilometers," Science (80-.). **356**(6343), 1140–1144 (2017).
28. S. K. Liao, W. Q. Cai, J. Handsteiner, B. Liu, J. Yin, L. Zhang, D. Rauch, M. Fink, J. G. Ren, W. Y. Liu, Y. Li, Q. Shen, Y. Cao, F. Z. Li, J. F. Wang, Y. M. Huang, L. Deng, T. Xi, L. Ma, T. Hu, L. Li, N. Le Liu, F. Koidl, P. Wang, Y. A. Chen, X. Bin Wang, M. Steindorfer, G. Kirchner, C. Y. Lu, R. Shu, R. Ursin, T. Scheidl, C. Z. Peng, J. Y. Wang, A. Zeilinger, and J. W. Pan, "Satellite-Relayed Intercontinental Quantum Network," Phys. Rev. Lett. **120**(3), 30501 (2018).
29. S.-K. Liao, W.-Q. Cai, W.-Y. Liu, L. Zhang, Y. Li, J.-G. Ren, J. Yin, Q. Shen, Y. Cao, Z.-P. Li, F.-Z. Li, X.-W. Chen, L.-H. Sun, J.-J. Jia, J.-C. Wu, X.-J. Jiang, J.-F. Wang, Y.-M. Huang, Q. Wang, Y.-L. Zhou, L. Deng, T. Xi, L. Ma, T. Hu, Q. Zhang, Y.-A. Chen, N.-L. Liu, X.-B. Wang, Z.-C. Zhu, C.-Y. Lu, R. Shu, C.-Z. Peng, J.-Y. Wang, and J.-W. Pan, "Satellite-to-ground quantum key distribution," Nature **549**(7670), 43–47 (2017).
30. S.-K. Liao, J. Lin, J.-G. Ren, W.-Y. Liu, J. Qiang, J. Yin, Y. Li, Q. Shen, L. Zhang, X.-F. Liang, H.-L. Yong, F.-Z. Li, Y.-Y. Yin, Y. Cao, W.-Q. Cai, W.-Z. Zhang, J.-J. Jia, J.-C. Wu, X.-W. Chen, S.-C. Zhang, X.-J. Jiang, J.-F. Wang, Y.-M. Huang, Q. Wang, L. Ma, L. Li, G.-S. Pan, Q. Zhang, Y.-A. Chen, C.-Y. Lu, N.-L. Liu, X. Ma, R. Shu, C.-Z. Peng, J.-Y. Wang, and J.-W. Pan, "Space-to-Ground Quantum Key Distribution Using a Small-Sized Payload on Tiangong-2 Space Lab," Chinese Phys. Lett. **34**(9), 090302 (2017).
31. G. Vallone, D. Dequal, M. Tomasin, F. Vedovato, M. Schiavon, V. Luceri, G. Bianco, and P. Villoresi, "Interference at the Single Photon Level Along Satellite-Ground Channels," Phys. Rev. Lett. **116**(25), 1–6 (2016).
32. G. Vallone, D. G. Marangon, M. Canale, I. Savorgnan, D. Bacco, M. Barbieri, S. Calimani, C. Barbieri, N. Laurenti, and P. Villoresi, "Adaptive real time selection for quantum key distribution in lossy and turbulent free-space channels," Phys. Rev. A **91**(4), 042320 (2015).
33. H. Takenaka, A. Carrasco-Casado, M. Fujiwara, M. Kitamura, M. Sasaki, and M. Toyoshima, "Satellite-to-ground quantum-limited communication using a 50-kg-class microsatellite," Nat. Photonics **11**(8), 502–508 (2017).
34. A. Villar, A. Lohrmann, X. Bai, T. Vergoossen, R. Bedington, C. Perumangatt, H. Y. Lim, T. Islam, A. Reezwana, Z. Tang, R. Chandrasekara, S. Sachidananda, K. Durak, C. F. Wildfeuer, D. Griffin, D. K. L. Oi, and A. Ling, "Entanglement demonstration on board a nano-satellite," Optica **7**(7), 734 (2020).
35. A. K. Majumdar and J. C. Ricklin, *Free-Space Laser Communications* (Springer New York, 2008).
36. J. Jin, S. Agne, J. P. Bourgoin, Y. Zhang, N. Lütkenhaus, and T. Jennewein, "Demonstration of analyzers for multimode photonic time-bin qubits," Phys. Rev. A **97**(4), 1–10 (2018).
37. E. Kerstel, A. Gardelein, M. Barthelemy, M. Fink, S. K. Joshi, and R. Ursin, "Nanobob: A CubeSat mission concept for quantum communication experiments in an uplink configuration," EPJ Quantum Technol. **5**(1), 1–34 (2018).
38. M. Toyoshima, H. Takenaka, Y. Shoji, Y. Takayama, Y. Koyama, and H. Kunimori, "Polarization measurements through space-to-ground atmospheric propagation paths by using a highly polarized laser source in space," Opt. Express **17**(25), 22333 (2009).
39. P. Sibson, C. Erven, M. Godfrey, S. Miki, T. Yamashita, M. Fujiwara, M. Sasaki, H. Terai, M. G. Tanner, C. M. Natarajan, R. H. Hadfield, J. L. O'Brien, and M. G. Thompson, "Chip-based quantum key distribution," Nat. Commun. **8**(1), 13984 (2017).
40. J. Jin, J.-P. Bourgoin, R. Tannous, S. Agne, C. J. Pugh, K. B. Kuntz, B. L. Higgins, and T. Jennewein, "Genuine time-bin-encoded quantum key distribution over a turbulent depolarizing free-space channel," Opt. Express **27**(26), 37214 (2019).
41. D. Stucki, N. Brunner, N. Gisin, V. Scarani, and H. Zbinden, "Fast and simple one-way quantum key distribution," Appl. Phys. Lett. **87**(19), 1–3 (2005).

42. A. Boaron, B. Korzh, R. Houlmann, G. Boso, D. Rusca, S. Gray, M. J. Li, D. Nolan, A. Martin, and H. Zbinden, "Simple 2.5 GHz time-bin quantum key distribution," Appl. Phys. Lett. **112**(17), 1–5 (2018).
43. G. L. Roberts, M. Lucamarini, J. F. Dynes, S. J. Savory, Z. L. Yuan, and A. J. Shields, "Modulator-Free Coherent-One-Way Quantum Key Distribution," Laser Photonics Rev. **11**(4), 1–4 (2017).
44. M. Chen, C. Liu, and H. Xian, "Experimental demonstration of single-mode fiber coupling over relatively strong turbulence with adaptive optics," Appl. Opt. **54**(29), 8722 (2015).
45. D. Dequal, L. T. Vidarte, V. R. Rodriguez, G. Vallone, P. Villoresi, A. Leverrier, and E. Diamanti, "Feasibility of satellite-to-ground continuous-variable quantum key distribution," arXiv 1–13 (2020).
46. C. Cahall, N. T. Islam, D. J. Gauthier, and J. Kim, "Multimode Time-Delay Interferometer for Free-Space Quantum Communication," Phys. Rev. Appl. **13**(2), 024047 (2020).
47. A. Biswas, M. Srinivasan, R. Rogalin, S. Piazzolla, J. Liu, B. Schratz, A. Wong, E. Alerstam, M. Wright, W. T. Roberts, J. Kovalik, G. Ortiz, A. Na-Nakornpanom, M. Shaw, C. Okino, K. Andrews, M. Peng, D. Orozco, and W. Klipstein, "Status of NASA's deep space optical communication technology demonstration," in *2017 IEEE International Conference on Space Optical Systems and Applications (ICSOS)* (IEEE, 2017), pp. 23–27.
48. G. S. Buller and R. J. Collins, "Single-photon generation and detection," Meas. Sci. Technol. **21**(1), 012002 (2010).
49. M. Buttafava, F. Villa, M. Castello, G. Tortarolo, E. Conca, M. Sanzaro, S. Piazza, P. Bianchini, A. Diaspro, F. Zappa, G. Vicidomini, and A. Tosi, "SPAD-based asynchronous-readout array detectors for image-scanning microscopy," Optica **7**(7), 755 (2020).
50. I. Gyongy, N. Calder, A. Davies, N. A. W. Dutton, R. R. Duncan, C. Rickman, P. Dalgarno, and R. K. Henderson, "A 256 x 256 , 100-kfps, 61% Fill-Factor SPAD Image Sensor for Time-Resolved Microscopy Applications," IEEE Trans. Electron Devices **65**(2), 547–554 (2018).
51. I. Takai, H. Matsubara, M. Soga, M. Ohta, M. Ogawa, and T. Yamashita, "Single-Photon Avalanche Diode with Enhanced NIR-Sensitivity for Automotive LIDAR Systems," Sensors **16**(4), 459 (2016).
52. P. W. R. Connolly, X. Ren, R. K. Henderson, and G. S. Buller, "Hot pixel classification of single-photon avalanche diode detector arrays using a log-normal statistical distribution," Electron. Lett. **55**(18), 1004–1006 (2019).
53. K. Ito, Y. Otake, Y. Kitano, A. Matsumoto, J. Yamamoto, T. Ogasahara, and H. Hiyama, "A Back Illuminated 10μm SPAD Pixel Array Comprising Full Trench Isolation and Cu-Cu Bonding with Over 14 % PDE at 940nm," IEEE Int. Electron Devices Meet. 347–350 (2020).
54. I. M. Antolović, A. C. Ulku, E. Kizilkan, S. Lindner, F. Zanella, R. Ferrini, M. Schnieper, E. Charbon, and C. Bruschini, "Optical-stack optimization for improved SPAD photon detection efficiency," in *Quantum Sensing and Nano Electronics and Photonics XVI*, M. Razeghi, J. S. Lewis, G. A. Khodaparast, and E. Tournié, eds. (SPIE, 2019), p. 99.
55. P. W. R. Connolly, X. Ren, A. McCarthy, H. Mai, F. Villa, A. J. Waddie, M. R. Taghizadeh, A. Tosi, F. Zappa, R. K. Henderson, and G. S. Buller, "High concentration factor diffractive microlenses integrated with CMOS single-photon avalanche diode detector arrays for fill-factor improvement," Appl. Opt. **59**(14), 4488 (2020).
56. K. Morimoto and E. Charbon, "High fill-factor miniaturized SPAD arrays with a guard-ring-sharing technique," Opt. Express **28**(9), 13068 (2020).
57. N. A. W. Dutton, I. Gyongy, L. Parmesan, S. Gnecchi, N. Calder, B. R. Rae, S. Pellegrini, L. A. Grant, and R. K. Henderson, "A SPAD-based QVGA image sensor for single-photon counting and quanta imaging," IEEE Trans. Electron Devices **63**(1), 189–196 (2016).
58. T. Al Abbas, N. A. W. Dutton, O. Almer, N. Finlayson, F. M. Della Rocca, and R. Henderson, "A CMOS SPAD Sensor with a Multi-Event Folded Flash Time-to-Digital Converter for Ultra-Fast Optical Transient Capture," IEEE Sens. J. **18**(8), 3163–3173 (2018).
59. C. Bonato, A. Tomaello, V. Da Deppo, G. Naletto, and P. Villoresi, "Feasibility of satellite quantum key distribution," New J. Phys. **11**(4), 045017 (2009).
60. H. Mishina and T. Asakura, "Two gaussian beam interference," Nouv. Rev. d'Optique **5**(2), 101–107 (1974).
61. F. Fidler, M. Knapek, J. Horwath, and W. R. Leeb, "Optical communications for high-altitude platforms," IEEE J. Sel. Top. Quantum Electron. **16**(5), 1058–1070 (2010).
62. P. J. Clarke, R. J. Collins, P. A. Hiskett, M.-J. García-Martínez, N. J. Krichel, A. McCarthy, M. G. Tanner, J. A. O'Connor, C. M. Natarajan, S. Miki, M. Sasaki, Z. Wang, M. Fujiwara, I. Rech, M. Ghioni, A. Gulinatti, R. H. Hadfield, P. D. Townsend, and G. S. Buller, "Analysis of detector performance in a gigahertz clock rate quantum key distribution system," New J. Phys. **13**, 23 (2011).
63. A. Maccarone, F. Mattioli Della Rocca, A. McCarthy, R. Henderson, and G. S. Buller, "Three-dimensional imaging of stationary and moving targets in turbid underwater environments using a single-photon detector array," Opt. Express **27**(20), 28437 (2019).